Analysis and suppression of wave-front-aberration phase noise in weak-equivalence-principle tests using dual-species atom interferometers

Jiangong Hu,[1] Xi Chen,[1,2,*] Jie Fang,[1] Lin Zhou,[1,2] Jiaqi Zhong,[1,2] Jin Wang,[1,2,†] and Mingsheng Zhan[1,2,‡]

[1]*State Key Laboratory of Magnetic Resonance and Atomic and Molecular Physics, Wuhan Institute of Physics and Mathematics, Chinese Academy of Sciences–Wuhan National Laboratory for Optoelectronics, Wuhan 430071, China*

[2]*Center for Cold Atom Physics, Chinese Academy of Sciences, Wuhan 430071, China*

(Received 22 June 2017; published 21 August 2017)

The wave-front aberration of Raman beams induces phase noise in atom interferometers and thus limits the performance of atom interferometers. We theoretically analyze the wave-front-aberration phase noise in weak-equivalence-principle tests using dual-species atom interferometers, and propose an expansion-rate-selection method to suppress the wave-front-aberration phase noise in both isotopic and nonisotopic atom interferometers. The suppression ratio is about 10 at the expense of half the number of atoms. The simulation based on appropriate experimental parameters shows that the wave-front aberration caused standard deviations to the Eötvös coefficient in weak-equivalence-principle tests using ^{85}Rb-^{87}Rb and ^{41}K-^{87}Rb are 1.3×10^{-14} and 3.0×10^{-13}. Better results can be obtained by improving the wave-front quality and utilizing atom cloud with lower temperature. The analysis and suppression of wave-front-aberration phase noise will be useful for the design of high-precision atom interferometer–based weak-equivalence-principle tests both on ground and in space.

DOI: 10.1103/PhysRevA.96.023618

I. INTRODUCTION

Atom interferometers (AIs) [1–3] have been widely used in fundamental physical experiments, such as precision measurements of gravity [4–10], rotation [11–13], and gravitational redshift [14], determinations of the Newtonian gravitational constant [15,16] and the fine structure constant [17,18], and tests of the post-Newtonian gravity [19] and the weak equivalence principle (WEP) [20–25]. In AI-based WEP tests, some measurement noises and systematic errors caused by gravity gradient, vibration, and rotation [26,27] are eliminated by sharing common Raman beams and by manipulating the dual-species atoms synchronously. The errors caused by Zeeman shift and ac Stark shift are eliminated by using same internal state configuration, such as double Raman transition [28] and double Bragg diffraction [29]. Presently, the lowest uncertainty of the WEP tests using dual-species AI is 3×10^{-8} [20]. It is necessary to further improve the precision of AI-based WEP tests in the microscopic particle domain. The precision of an AI is inversely proportional to the square of the free evolution time of atoms, therefore, several long-baseline atom interferometers [30–32] were built to improve the precision of WEP tests. In the space microgravity environment, it is possible to prepare atom clouds with lower temperature and to further extend the free evolution time of an AI, thus AI-based WEP tests [27,33] in space are expected to achieve higher precision. However, there are still key problems in both long-baseline AIs and space AIs, one of the most prominent of these problems is the wave-front aberration of Raman beams [27]. When Raman beams interact with atoms, the wave-front aberration is printed on the atomic wave function, and thus induces the phase shift in AIs. Louchet-Chauvet *et al.* measured this phase noise by extrapolating its temperature dependence [34]. Schkolnik *et al.* investigated the effect of wave-front aberration in atom intererometry [35]. Zhou *et al.* measured the effect of wave-front aberrations in an AI by modulating the diameter of Raman beams [36]. In spite of this progress, to further solve this key problem, an intensive analysis and an effective suppression for wave-front-aberration phase noise (WAPN) are still urgently needed. In this paper, we theoretically analyze the influence of the wave-front aberration in WEP tests using dual-species ^{85}Rb-^{87}Rb and ^{41}K-^{87}Rb AI, and propose an expansion-rate-selection method to suppress the WAPN in both isotopic and nonisotopic AI-based WEP tests.

II. WAVE-FRONT-ABERRATION PHASE NOISE

A. The phase of the Gaussian beam

In AIs, the Raman laser beam is usually composed of two counterpropagating Gaussian beams with a fixed frequency difference. Assume a Gaussian beam with wavelength of λ and waist radius of ω_0 propagates along the z direction, and the waist center is located at the origin of coordinates. By solving the paraxial Helmholtz equation, the electric field of the Gaussian beam is

$$E(x,y,z) = E_0 \frac{\omega_0}{\omega(z)} \exp\left[i\phi_{\mathrm{B}}(x,y,z) - \frac{x^2+y^2}{\omega^2(z)} \right], \quad (1)$$

where E_0 is the electric field intensity at the beam waist center, $k = 2\pi/\lambda$ is the wave vector, $\omega(z) = \omega_0\sqrt{1+(z/z_R)^2}$ is the beam radius at position z, $z_R = \pi\omega_0^2/\lambda$ is the Rayleigh length, $R(z) = z[1+(z_R/z)^2]$ is the radius of wave-front curvature, and $\phi_{\mathrm{B}}(x,y,z)$ is the phase of the Gaussian beam. $\phi_{\mathrm{B}}(x,y,z)$ is described as

$$\phi_{\mathrm{B}}(x,y,z) \equiv kz + k(x^2+y^2)/2R(z) - \arctan(z/z_R), \quad (2)$$

where the linear phase kz is only related to z and k; the curvature phase $k(x^2+y^2)/2R(z)$ is proportional to the square of radial distance, it has maximum value at $z = z_R$, and

*chenxi@wipm.ac.cn
†wangjin@wipm.ac.cn
‡mszhan@wipm.ac.cn

it has zero value at $z = 0$ and $z \to \infty$; the Gouy phase, $\arctan(z/z_R)$, is zero at $z = 0$, and it gradually tends to $\pi/2$ when $z \to \infty$. Define the linear phase of the Gaussian beam as $\phi_{\mathrm{B,lin}}(x,y,z) \equiv kz$, and the evolution phase of the Gaussian beam is

$$\phi_{\mathrm{B,evol}}(x,y,z) \equiv \frac{k(x^2+y^2)}{2[R(z)]} - \arctan(z/z_R). \tag{3}$$

B. The wave-front-aberration induced phase noise

Ideally, the Raman beam's phase only contains the phases of the Gaussian beams. However, actual imperfect optics usually induce additional phases. When the incident Gaussian beams pass through optics (such as the windows of the vacuum chamber, the $\lambda/4$ wave plates, and the retro-reflecting mirrors) to form the Raman beam, the aberration of these optics is transferred to the wave front of the Raman beam. Here, we take the influences of all the optics as a whole, and select a linear combination of Zernike polynomials in the Cartesian coordinates to characterize the wave-front aberration of a Gaussian beam. The phase induced by wave-front aberration $\phi_{\mathrm{B,ini}}(x,y)$ is expressed as

$$\phi_{\mathrm{B,ini}}(x,y) = \sum_{i=1}^{n} a_i Z_i(x,y), \tag{4}$$

where $Z_i(x,y)$ is the ith order normalized Zernike polynomials, a_i is the corresponding coefficient, and n is the maximum order number of Zernike polynomials.

C. The evolution of wave-front-aberration phase noise

Similar to the evolution phase of a Gaussian beam, the aberration phase also varies with location. This effect has not been studied in AIs, and has to be investigated in detail for high-precision AI-based WEP tests. The electric field of the Gaussian beam is

$$E(x,y,z) = E_0(x,y,z)\exp[i\phi(x,y,z)], \tag{5}$$

where $E_0(x,y,z)$ and $\phi(x,y,z)$ are the intensity and the phase of the electric field. According to Huygens-Kirchhoff diffraction integral formula [37] and the paraxial approximation condition, the electric field is

$$E(x,y,z) = \iint E(x',y',0)h(x-x',y-y')dx'dy', \tag{6}$$

where $E(x',y',0) = E_0(x',y',0)\exp(i\phi(x',y',0))$ is the electric field at $z' = 0$, $\phi(x',y',0)$ is the corresponding phase, z is the distance from the initial plane, and $h(x-x',y-y')$ is the transfer function of the electric field evolving in the space domain. This transfer function has the following form:

$$h(x,y) = \frac{z}{i\lambda}\frac{\exp(ikr)}{r^2}, \tag{7}$$

where $r = \sqrt{x^2+y^2+z^2}$. Based on Eq. (6) and a given initial value, the electric field at an arbitrary position can be solved. By determining the angle of $E(x,y,z)$, the phase $\phi(x,y,z)$ can be obtained. Equation (6) is a two-dimensional convolution in the space domain. This calculation is quite complex, especially when the initial electric field has an extraordinary form. To simplify this calculation, we transfer Eq. (6) into the frequency domain by using the Fourier transformation, where the convolution in the space domain was converted to the product calculation in the frequency domain. Then, an inverse Fourier transformation is applied to transfer the electric field back to the space domain. This procedure is expressed as

$$\begin{aligned} E(x,y,z) &= \iint E(x',y',0)h(x-x',y-y')dx'dy' \\ &= F^{-1}\{F[E(x,y,0)]H(f_{\mathrm{X}},f_{\mathrm{Y}})\}, \end{aligned} \tag{8}$$

where $H(f_{\mathrm{X}},f_{\mathrm{Y}})$ is the transfer function in the frequency domain, and

$$\begin{aligned} H(f_{\mathrm{X}},f_{\mathrm{Y}}) &= F[h(x,y)] \\ &= \exp[ikz\sqrt{1-(\lambda f_{\mathrm{x}})^2-(\lambda f_{\mathrm{y}})^2}], \end{aligned} \tag{9}$$

F, F^{-1} represent the Fourier transformation and the inverse Fourier transformation. f_{x} and f_{y} are the frequencies in the space domain. Due to the complex form of the initial electric field, Eq. (8) can only be solved by using the numerical calculation.

D. The phase of the counterpropagating Raman beam

Suppose an ideal Gaussian beam propagates along the z direction, the beam waist overlaps with the retro-reflecting mirror, the waist center is located at $(0,0,0)$, as shown in Fig. 1. Assume the aberration is only induced by the retro-reflecting mirror, and the two counterpropagating Gaussian beams have the same frequency for simplicity. We ignore the constant π

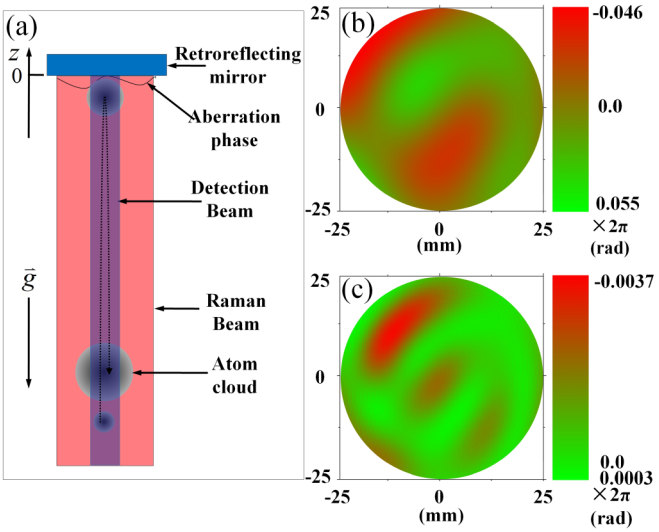

FIG. 1. A fountain-type AI and its aberration phase evolution. (a) The schematic diagram of a fountain-type AI. The atom cloud is launched upward from the bottom of the fountain. The Raman lasers are reflected by a retro-reflecting mirror. After interacting with the three pulses of the Raman laser, the atom cloud is detected by a detection beam in the vertical direction. (b) The simulated initial aberration phase $\phi_{\mathrm{B,ini}}$. The phase is randomly created by using 49 orders of Zernike polynomials; the peak to valley value of the aberration phase is $2\pi/10$ in a circular area with a radius of 25 mm. (c) The corresponding evolution of the aberration phase $\phi_{\mathrm{W,evol}}$ calculated from the initial aberration phase $\phi_{\mathrm{B,ini}}$ in (b). The evolution length is 10 m.

phase shift of the reflecting beam induced by the reflecting mirror. Then, the phase of the Raman beam is

$$\phi_{\mathrm{R}}(x,y,z) = \phi_{\mathrm{Inc}}(x,y,z) + \phi_{\mathrm{Ref}}(x,y,z), \tag{10}$$

where $\phi_{\mathrm{Inc}}(x,y,z) = \phi_{\mathrm{B}}(x,y,z)$ is the phase of the incident beam, and $\phi_{\mathrm{Ref}}(x,y,z) = -\phi_{\mathrm{B}}(x,y,-z) + \phi_{\mathrm{W}}(x,y,z)$ is the phase of the reflecting beam, $\phi_{\mathrm{W}}(x,y,z) \equiv \phi_{\mathrm{B,ini}}(x,y) + \phi_{\mathrm{W,evol}}(x,y,z)$ is the phase induced by wave-front aberration, $\phi_{\mathrm{B,ini}}(x,y)$ is the initial aberration phase induced by the retro-reflecting mirror, and $\phi_{\mathrm{W,evol}}(x,y,z)$ is the evolution of aberration phase. Equation (10) is rewritten as

$$\begin{aligned}\phi_{\mathrm{R}}(x,y,z) = {} & 2\phi_{\mathrm{B,lin}}(x,y,z) + 2\phi_{\mathrm{B,evol}}(x,y,z) \\ & + \phi_{\mathrm{B,ini}}(x,y) + \phi_{\mathrm{W,evol}}(x,y,z),\end{aligned} \tag{11}$$

where $\phi_{\mathrm{B,lin}}$ is the linear phase of the Gaussian beam, $\phi_{\mathrm{B,evol}}$, $\phi_{\mathrm{B,ini}}$, and $\phi_{\mathrm{W,evol}}$ are the nonlinear phases, and the overall nonlinear phase of the Raman beam is labeled as $\phi_{\mathrm{R,nl}}$.

E. The simulation of wave-front-aberration phase noise

With numerical simulation, we create a random initial aberration phase and calculate the evolution of its aberration phase. First, Eq. (4) is used to create an initial aberration phase $\phi_{\mathrm{B,ini}}$ at $z = 0$, where the Zernike polynomials $Z_i(x,y)$ are normalized to a unit circular area, and the coefficients a_i are random numbers with normal distribution. The average value of the distribution is 0, and the standard deviation is 1. To set the size and the peak to valley value of the aberration phase, the area of the phase plane is resized, and the amplitude is adjusted. Here, the area is a circular with a radius of 25 mm, and the peak-to-valley value is $2\pi/10$ for the 780-nm laser in this area; 49-order Zernike polynomials are used to create $\phi_{\mathrm{B,ini}}$. Then, the final phase $\phi(x,y,z)$ is derived by $E(x,y,0)$ at $z = 0$ by using Eq. (8). Finally, the evolution aberration phase $\phi_{\mathrm{W,evol}}$ is obtained by subtracting ϕ_{B} and $\phi_{\mathrm{B,ini}}$ from $\phi(x,y,z)$. Figure 1(b) is the simulated initial aberration phase, and Fig. 1(c) is the evolution of the aberration phase.

III. THE SYSTEMATIC ERROR IN WEP TESTS INDUCED BY THE RAMAN BEAM'S PHASE

A. The systematic error in gravity measurements

In a Mach-Zehnder-type AI, the atoms interact with a $\pi/2 - \pi - \pi/2$ Raman-pulse sequence. The interference phase of an individual atom is

$$\phi_{\mathrm{AI}}(\vec{r},\vec{v}) = \phi_{\mathrm{R}}(\vec{r_1}) + \phi_{\mathrm{R}}(\vec{r_3}) - 2\phi_{\mathrm{R}}(\vec{r_2}), \tag{12}$$

where $\vec{r}$ and $\vec{v}$ are the initial position and the velocity of the atom. $\vec{r_i} \equiv (x_i, y_i, z_i)(i = 1,2,3)$ is the position where the atom interacts with the ith Raman pulse. Assume the atom only feels gravity during its free fall, and the direction of gravity is along the z axis, the atom interacts with the first Raman pulse at t_0, and its free evolution time is T. The dependence of $\vec{r_i}$ on the initial position and the initial velocity is

$$\vec{r_i} = \vec{r} + \vec{v}[t_0 + (i-1)T] + \vec{g}[t_0 + (i-1)T]^2/2. \tag{13}$$

The interference phase of the individual atom is obtained by substituting Eqs. (13) and (11) into Eq. (12).

Atoms with different positions and velocities give different interference phases, and the phase of the atom cloud is the average of all atoms. The distributions of the velocity $p(\vec{v})$ and the position $f(\vec{r})$ of the atom cloud are

$$p(\vec{v}) = \prod_{i=x,y,z} \frac{1}{\sqrt{2\pi}\sigma_{v_i}} \exp\left[\frac{-(v_i - v_{0i})^2}{2(\sigma_{v_i})^2}\right], \tag{14a}$$

$$f(\vec{r}) = \prod_{i=x,y,z} \frac{1}{\sqrt{2\pi}\sigma_{r_i}} \exp\left[\frac{-(r_i - r_{0i})^2}{2(\sigma_{r_i})^2}\right], \tag{14b}$$

where σ_{r_i} and $\sigma_{v_i}(i = x,y,z)$ are the position uncertainty and the velocity uncertainty in the i direction; r_{0i} and v_{0i} are the averaged position and velocity in the i direction. For an atom cloud with temperature of T_i in the i direction, the corresponding velocity uncertainty is $\sigma_{v_i} = \sqrt{k_{\mathrm{B}}T_i/m}$, where k_{B} is the Boltzmann constant, and m is the mass of the atom. The Rabi frequency depends on the position of each individual atom; this results in a variety of fringe contrasts for a specific atom. But for our simulated experimental parameters, the size of the Raman beam is much larger than the atom cloud; a typical waist radius of the Raman beam is 25 mm, while the expansion radius of a 10-nK Rb atom cloud after 2.9-s free fall is about 3 mm, thus all atoms are involved and contribute to the average phase $\overline{\phi_{\mathrm{AI}}}$ with the same weight,

$$\overline{\phi_{\mathrm{AI}}} = \int_{\vec{r}}\int_{\vec{v}} \phi_{\mathrm{AI}}(\vec{r},\vec{v})p(\vec{v})f(\vec{r})d\vec{v}d\vec{r}. \tag{15}$$

By substituting Eq. (12) into Eq. (15), we calculate the phase $\overline{\phi_{\mathrm{AI}}}$, which is induced by the different terms in $\phi_{\mathrm{R}}(x,y,z)$. We find that the linear phase induced by $\phi_{\mathrm{R,lin}}$ is $\overline{\phi_{\mathrm{AI,lin}}} = k_{\mathrm{eff}}gT^2$, where $k_{\mathrm{eff}} \equiv 2k$ is the effective wave vector of the Raman beam. The nonlinear phase induced by $\phi_{\mathrm{R,nl}}$ is $\overline{\phi_{\mathrm{AI,nl}}}$, which induces a systematic error Δg_{rel} in relative gravity measurement, and

$$\Delta g_{\mathrm{rel}} = \frac{\Delta g}{g} = \frac{\overline{\phi_{\mathrm{AI,nl}}}}{k_{\mathrm{eff}}gT^2}. \tag{16}$$

B. The systematic error in WEP tests

In AI-based WEP tests, by synchronously measuring the gravitational acceleration $g_i(i = 1,2)$ of two-species atoms, we obtain the Eötvös coefficient, $\eta = (g_2 - g_1)/\bar{g}$, where $\bar{g} = (g_1 + g_2)/2$ is the average value of the accelerations. Assume $k_{\mathrm{eff},1}$ and $k_{\mathrm{eff},2}$ are effective wave vectors of two-species AIs, $\alpha = k_{\mathrm{eff},2}/k_{\mathrm{eff},1}$ is the ratio of two wave vectors, and the populations of inner states of two AIs are

$$P_1 = \tfrac{1}{2}[1 + \cos(k_{\mathrm{eff},1}g_1T^2 + \overline{\phi_{\mathrm{AI,nl},1}} + \phi_{\mathrm{scan},1})], \tag{17a}$$

$$P_2 = \tfrac{1}{2}[1 + \cos(k_{\mathrm{eff},2}g_2T^2 + \overline{\phi_{\mathrm{AI,nl},2}} + \phi_{\mathrm{scan},2})], \tag{17b}$$

where $\phi_{\mathrm{scan},i}(i = 1,2)$ are artificially introduced scanning phases.

By synchronously scanning the phase ($\phi_{\mathrm{scan}} = \phi_{\mathrm{scan},1} = \phi_{\mathrm{scan},2}$) and plotting $P_1(\phi_{\mathrm{scan}})$ versus $P_2(\phi_{\mathrm{scan}})$, an elliptic curve is obtained as shown in Fig. 2(a). The information of η is derived by the fitted differential phase of this elliptic curve. However, if $k_{\mathrm{eff},1}$ and $k_{\mathrm{eff},2}$ are different, their difference, $\Delta k_{\mathrm{eff}} = k_{\mathrm{eff},1} - k_{\mathrm{eff},2}$, gives a phase shift $\Delta k_{\mathrm{eff}}\bar{g}T^2$ [38], and the nonlinear phases of the AIs $\overline{\phi_{\mathrm{AI,nl},i}}(i = 1,2)$ are different. Two sets of Raman beams share the same retro-reflecting

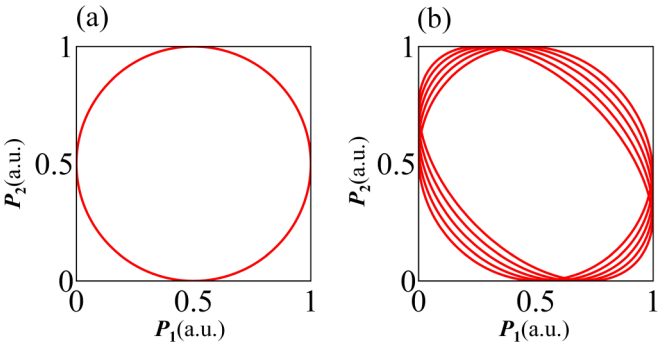

FIG. 2. The elliptic curve and the Lissajous curves. (a) The elliptic curve obtained by plotting $P_1(\phi_{\rm scan})$ versus $P_2(\phi_{\rm scan})$; the range of $\phi_{\rm scan}$ is 2π. (b) The Lissajous curve obtained by plotting $P_1(\phi_{\rm scan,1})$ versus $P_2(\phi_{\rm scan,1})$, the ratio of effect vectors is $\alpha = 780/767$, and the range of $\phi_{\rm scan,1}$ is 10π.

mirror, and the phase shift caused by the mirror aberration has the form $k_{{\rm eff},i}\Delta l (i = 1,2)$, where Δl represents the aberration deformation. The initial aberration phases $\phi_{{\rm W,ini},i} (i = 1,2)$ are related to α. If we directly subtract the phase difference between two AIs, there is an offset phase, which causes systematic error in WEP tests.

We utilize a proportional-scanning-phase method [38] to suppress the aberration phase shift. We scan phases with the same ratio as that of the effective wave vectors $\phi_{\rm scan,2}/\phi_{\rm scan,1} = \alpha$, and plot $P_1(\phi_{\rm scan})$ versus $P_2(\phi_{\rm scan})$, a Lissajous curve is obtained as shown in Fig. 2(b). Equation (17) is written as

$$P_1 = \tfrac{1}{2}[1 + \cos(\phi_{\rm com})], \tag{18a}$$

$$P_2 = \tfrac{1}{2}[1 + \cos(\alpha\phi_{\rm com} + \phi_{\rm diff})]. \tag{18b}$$

We define $\phi_{\rm com} \equiv k_{{\rm eff},1} g_1 T^2 + \overline{\phi_{{\rm AI,nl},1}} + \phi_{{\rm scan},1}$ as the common-mode phase, $\phi_{\rm diff} \equiv k_{{\rm eff},2}\eta\bar{g}T^2 + (\overline{\phi_{{\rm AI,nl},2}} - \alpha\overline{\phi_{{\rm AI,nl},1}})$ as the differential-mode phase, and $\phi_{\rm diff}$ is extracted by using the Bayesian estimation [38]. The first term of $\phi_{\rm diff}$ is the Eötvös coefficient phase, and the second term is the aberration phase. The systematic error of the WEP test induced by the nonlinear phase is

$$\Delta\eta = \frac{\overline{\phi_{{\rm AI,nl},2}}}{k_{{\rm eff},2}\bar{g}T^2} - \frac{\overline{\phi_{{\rm AI,nl},1}}}{k_{{\rm eff},1}\bar{g}T^2}. \tag{19}$$

If the ratio of $\overline{\phi_{{\rm AI,nl},i}} (i = 2,1)$ is α, it does not lead to a deviation of the WEP test. If $k_{{\rm eff},1} = k_{{\rm eff},2} = k_{\rm eff}$, Eq. (19) can be rewritten as

$$\Delta\eta = \frac{\overline{\phi_{{\rm AI,nl},2}} - \overline{\phi_{{\rm AI,nl},1}}}{k_{\rm eff}\bar{g}T^2}, \tag{20}$$

the Lissajous curve degrades to an elliptic curve, and the differential phase of the elliptic curve is derived by using the least squares fit [39] or the Bayesian estimation [40].

IV. THE SUPPRESSION OF THE WAVE-FRONT-ABERRATION PHASE NOISE IN WEP TESTS

A. The experimental parameters for the simulation

Here, we take the 10-meter-high atom fountains [30–32] for simulation. Suppose the local gravity is $g = 10$ m/s^2, the dual-species atom clouds have the same temperature, and the temperature varies from 1 to 20 nK. The atom clouds are launched upwards from the bottom of the fountain, after a free-fall time of $t_0 = 0.1$ s; the atoms interact with the first Raman pulse. The maximum free evolution time is 1.4 s, the wavelengths of the Raman beams are 780 nm for Rb isotopes, and 767 nm for ^{41}K, and the waist radius of each Raman beam is 25 mm.

For the 780-nm Raman beam, the initial aberration phase $\phi_{\rm B,ini,1}$ has a peak-to-valley value of $2\pi/10$ within a 25-mm-radius circular area. For the 767-nm Raman beam, the initial aberration phase $\phi_{\rm B,ini,2}$ is proportional to $\phi_{\rm B,ini,1}$, $\phi_{\rm B,ini,2} = (780/767)\phi_{\rm B,ini,1}$. The evolution phases of Gaussian beams are noted as $\phi_{{\rm W,evol},i} (i = 1$ for 780 nm, $i = 2$ for 767 nm).

B. The simulation results and discussion

First, Eq. (16) is used to calculate $\Delta g_{\rm rel}$ for ^{85}Rb, ^{87}Rb, and ^{41}K atoms for different temperatures, where specific $\phi_{\rm B,ini}$ and $\phi_{\rm W,evol}$ are used. Figure 3 shows $\Delta g_{\rm rel}$ induced by different terms of the $\phi_{\rm R,nl}$ for ^{85}Rb and ^{41}K atoms. $\Delta g_{\rm rel}$ for ^{87}Rb atoms are quite similar to that for ^{85}Rb atoms, so we do not show the picture here.

According to Fig. 3, for both the ^{85}Rb and ^{41}K AI, (1) $\phi_{{\rm B,evol},i}$ introduces relatively large offsets of $\Delta g_{\rm rel}$. The offsets, which were mainly induced by the Gouy phases, are nearly independent of temperature. The contribution of the curvature

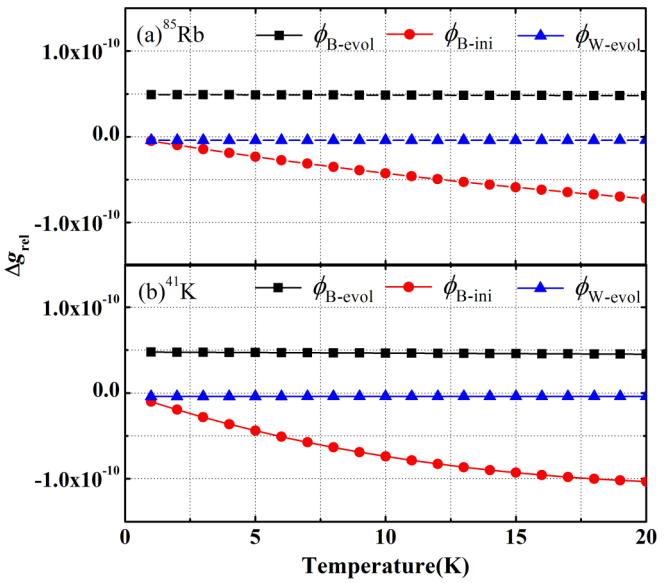

FIG. 3. The offset of the relative gravity measurement $\Delta g_{\rm rel}$ versus the temperature. $\Delta g_{\rm rel}$ induced by the nonlinear phase of the Raman lasers $\phi_{\rm R,nl}$ is calculated using the experimental parameters, the specific $\phi_{{\rm B,ini},i}$ and $\phi_{{\rm W,evol},i}$ in Sec. IV A. (a) For the ^{85}Rb atom interferometer. (b) For the ^{41}K atom interferometer.

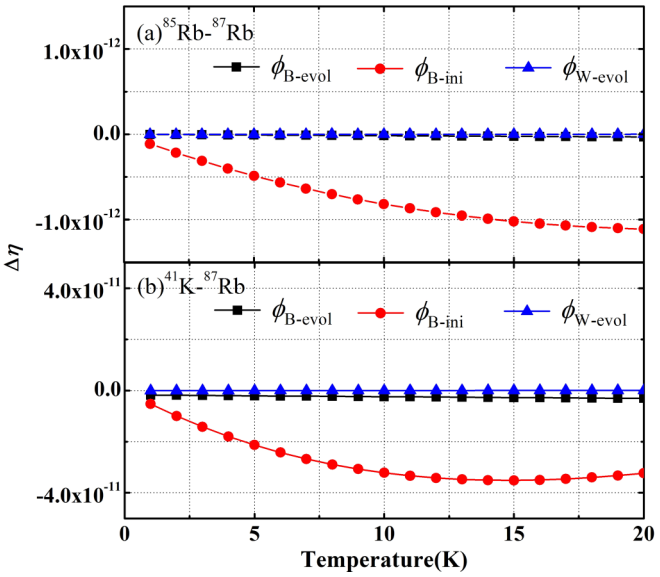

FIG. 4. The dependence of systematic error $\Delta\eta$ on the temperature. $\Delta\eta$ induced by terms of the nonlinear phase of Raman beams $\phi_{\mathrm{R,nl}}$ is calculated using the experimental parameters, and the specific $\phi_{\mathrm{B,ini},i}$ and $\phi_{\mathrm{W,evol},i}$ in Sec. IV A. (a) For ^{85}Rb-^{87}Rb. (b) For ^{41}K-^{87}Rb.

phases is quite small. (2) Δg_{rel} induced by $\phi_{\mathrm{B,ini},i}$ increases with the temperature, and tunes to zero when the temperature is zero, because the atom clouds expand with time, and the phases at three Raman pulses are different; the higher the temperature is, the larger the offset will be. (3) Δg_{rel} induced by $\phi_{\mathrm{W,evol},i}$ is relatively smaller than that by the other two terms, and the induced offsets are nearly independent of temperature.

Then, Eq. (19) is used to calculate $\Delta\eta$ with the same $\phi_{\mathrm{B,ini},i}$ and $\phi_{\mathrm{W,evol},i}$. Figure 4 shows $\Delta\eta$ induced by different terms of $\phi_{\mathrm{R,nl}}$, and compared with Δg_{rel}, $\Delta\eta$ induced by $\phi_{\mathrm{B,evol},i}$ is greatly suppressed. For ^{85}Rb-^{87}Rb, the wavelengths of the Raman beams, $\Delta\eta$ induced by the Gouy phases, the expansion rates, and the atom masses are almost exactly the same. For ^{41}K-^{87}Rb, most part of $\Delta\eta$ induced by the Gouy phases is common mode, but the wavelengths of the Raman beams and the expansion rates are different, and $\Delta\eta$ induced by the curvature phase is not strictly common mode. However the contribution of the curvature phase is too small to be considered in simulation. For both atom pairs, $\Delta\eta$ induced by $\phi_{\mathrm{B,ini},i}$ are suppressed and the suppression ratio for ^{85}Rb-^{87}Rb is much higher than that for ^{41}K-^{87}Rb. $\Delta\eta$ induced by $\phi_{\mathrm{W,evol},i}$ is much smaller than that by the two previous terms.

To verify the reliability of the simulation, we randomly create 10 individual values of $\phi_{\mathrm{B,ini},i}$, derive the corresponding $\phi_{\mathrm{W,evol},i}$, and calculate the average values and standard deviations of $\Delta\eta$ induced by different nonlinear phases. Table I shows the calculation results of the Δg_{rel} for atoms ^{85}Rb, ^{87}Rb, and ^{41}K; the temperature of the atom clouds is set to be 10 nK. Because $\phi_{\mathrm{B,evol},i}$ are constants for the 10 cases, Δg_{rel} induced by $\phi_{\mathrm{B,evol},i}$ are also constants; the standard deviation of this term is not listed in Table I. Because of the random creations of the $\phi_{\mathrm{B,ini},i}$, the expected average values of Δg_{rel} induced by

TABLE I. The average values (AV) and the standard deviations (SD) of Δg_{rel} induced by the nonlinear phase terms of the Raman lasers $\phi_{\mathrm{R,nl}}$. Ten individual random $\phi_{\mathrm{B,ini},i}$ and corresponding $\phi_{\mathrm{W,evol},i}$ are used for the calculation. The calculation is based on ^{85}Rb, ^{87}Rb, and ^{41}K atom interferometers. The temperature of the atoms is set as 10 nK.

	^{85}Rb	^{87}Rb	^{41}K
$\phi_{\mathrm{B,evol}}$(AV)	4.9×10^{-11}	4.9×10^{-11}	4.6×10^{-11}
$\phi_{\mathrm{B,ini}}$(SD)	4.0×10^{-11}	4.0×10^{-11}	6.7×10^{-11}
$\phi_{\mathrm{W,evol}}$(SD)	1.7×10^{-12}	1.7×10^{-12}	1.5×10^{-12}
$\phi_{\mathrm{R,nl}}$(SD)	4.1×10^{-11}	4.0×10^{-11}	6.7×10^{-11}

$\phi_{\mathrm{B,ini},i}$ and $\phi_{\mathrm{W,evol},i}$ are zero, so the average values of these two terms are not listed in Table I too.

According to Table I, the standard deviation of the Δg_{rel} induced by the overall $\phi_{\mathrm{R,nl},i}$ for ^{85}Rb, ^{87}Rb, and ^{41}K are 4.1×10^{-11}, 4.0×10^{-11}, and 6.7×10^{-11}, which are mainly contributed by $\phi_{\mathrm{B,ini},i}$. Δg_{rel} induced by $\phi_{\mathrm{B,evol},i}$ are 4.9×10^{-11}, 4.9×10^{-11}, and 4.6×10^{-11}, respectively.

Table II shows the average values and standard deviations of $\Delta\eta$ for ^{85}Rb-^{87}Rb and ^{41}K-^{87}Rb. The suppression ratio γ is used to quantify the suppression effect of $\Delta\eta$, and it is defined as

$$\gamma = \left|\frac{\Delta g_{\mathrm{rel},1} + \Delta g_{\mathrm{rel},2}}{2\Delta\eta}\right|. \tag{21}$$

The standard deviations of $\Delta\eta$ induced by the overall $\phi_{\mathrm{R,nl},i}$ (mainly contributed by $\phi_{\mathrm{B,ini},i}$) for ^{85}Rb-^{87}Rb and ^{41}K-^{87}Rb are 7.3×10^{-13} and 2.7×10^{-11}, respectively. The corresponding suppression ratios are 56 and 2.0. $\Delta\eta$ induced by $\phi_{\mathrm{B,evol},i}$ for ^{85}Rb-^{87}Rb and ^{41}K-^{87}Rb are -1.5×10^{-14} and -2.4×10^{-12}; the corresponding suppression ratios are 3200 and 20. A fix systematic error of the order 10^{-12} is introduced in the ^{41}K-^{87}Rb WEP tests due to the different wavelengths of the Raman lasers.

We also calculate $\Delta\eta$ using 1-nK atom clouds. The standard deviations of the Δg_{rel} induced by the overall $\phi_{\mathrm{R,nl},i}$ for atom ^{85}Rb, ^{87}Rb, and ^{41}K are 5.9×10^{-12}, 5.8×10^{-12} and 1.1×10^{-11}, respectively. The standard deviations of $\Delta\eta$ induced by $\phi_{\mathrm{R,nl},i}$ for ^{85}Rb-^{87}Rb and ^{41}K-^{87}Rb are 1.1×10^{-13} and 5.1×10^{-12}; the corresponding γ are 53 and 1.6. For both the relative gravity measurement and the WEP test experiments,

TABLE II. The average value (AV), the standard deviation (SD), and the suppression ratio (γ) of $\Delta\eta$ induced by the nonlinear phases. Ten individual random $\phi_{\mathrm{B,ini},i}$ and corresponding $\phi_{\mathrm{W,evol},i}$ are used for the calculation. The calculation is based on atom pairs of ^{85}Rb-^{87}Rb and ^{41}K-^{87}Rb. The temperature of atoms is set as 10 nK.

	^{85}Rb-^{87}Rb	γ	^{41}K-^{87}Rb	γ
$\phi_{\mathrm{B,evol}}$(AV)	-1.5×10^{-14}	3200	-2.4×10^{-12}	20
$\phi_{\mathrm{B,ini}}$(SD)	7.3×10^{-13}	54	2.7×10^{-11}	1.9
$\phi_{\mathrm{W,evol}}$(SD)	9.2×10^{-15}	180	2.9×10^{-13}	5.5
$\phi_{\mathrm{R,nl}}$(SD)	7.3×10^{-13}	56	2.7×10^{-11}	2.0

the standard deviations are improved by about 7 times, while the suppression ratios of $\Delta\eta$ are nearly unchanged.

C. The expansion-rate-selection method

From the above simulation, two problems limit the reduction of the $\Delta\eta$. First, the wavelengths of the Raman beams for ^{41}K-^{87}Rb are different, thus the Gouy phases induced Δg_{rel} are not common mode, which introduces systematic error in WEP tests. To solve this problem, we optimize the waist radii of the Raman beams to induce the same Δg_{rel}. We set the waist radius for the 780-nm Raman beam as 25.00 mm, and that for the 766-nm Raman beam is calculated to be 24.57 mm. Second, the expansion rates of the atom clouds are different for both ^{85}Rb-^{87}Rb and ^{41}K-^{87}Rb; Δg_{rel} induced by $\phi_{\mathrm{B,ini},i}$ are only partially common mode, which limits the suppression ratios. Therefore, it is necessary to make the atom clouds have more consistent expansion rates. To solve this problem, we select the expansion rates by only detecting the atoms in a specific area. We use the beams that propagate along the z direction to detect the two atom clouds after the interference process, the axis of the beams coincides with the centers of the atom clouds, and the two detection beams have the same radius, thus only part of the atoms with the same expansion rate in the clouds can be detected; atoms with different expansion rates are excluded from the detection area. In this case, Eq. (15) needs to be modified to calculate $\overline{\phi_{\mathrm{AI}}}$,

$$\overline{\phi_{\mathrm{AI}}} = \frac{\int_{\vec{r}}\int_{\sqrt{v_x^2+v_y^2}<v_{\mathrm{sel}}} \phi_{\mathrm{AI}}(\vec{r},\vec{v})p(\vec{v})f(\vec{r})d\vec{v}d\vec{r}}{\int_{\vec{r}}\int_{\sqrt{v_x^2+v_y^2}<v_{\mathrm{sel}}} p(\vec{v})f(\vec{r})d\vec{v}d\vec{r}}, \tag{22}$$

where $v_{\mathrm{sel}} = r_{\mathrm{det}}/(2T + t_0)$ is the maximum transverse velocity of detectable atoms, and r_{det} is the radius of the detection beam. The detection ratio, $\beta \equiv \int_{\vec{r}}\int_{\sqrt{v_x^2+v_y^2}<v_{\mathrm{sel}}} p(\vec{v})f(\vec{r})d\vec{v}d\vec{r}$, indicates the proportion of detectable atoms.

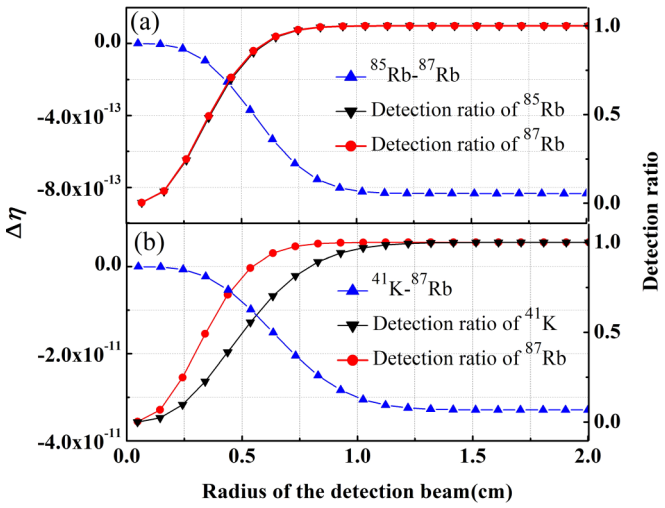

FIG. 5. The dependence of the systematic error $\Delta\eta$ and the detection ratio β on the radius of the detection beam r_{det}. The parameters and the specific $\phi_{\mathrm{B,ini},i}$ and $\phi_{\mathrm{W,evol},i}$ in Sec. IV A are used in the simulation. The temperatures of the atom clouds are set to be 10 nK. (a) For ^{85}Rb-^{87}Rb. (b) For ^{41}K-^{87}Rb.

TABLE III. The average values (AV), the standard deviations (SD) and the suppression ratios (γ) of $\Delta\eta$ induced by the nonlinear phases with the expansion-rate-selection method.

	^{85}Rb-^{87}Rb	γ	^{41}K-^{87}Rb	γ
$\phi_{\mathrm{B,evol}}$(AV)	-1.4×10^{-15}	36000	-4.3×10^{-14}	1100
$\phi_{\mathrm{B,ini}}$(SD)	9.1×10^{-14}	440	2.2×10^{-12}	24
$\phi_{\mathrm{W,evol}}$(SD)	1.6×10^{-15}	1000	4.5×10^{-14}	35
$\phi_{\mathrm{R,nl}}$(SD)	9.1×10^{-14}	450	2.2×10^{-12}	25

D. The simulation results using the expansion-rate-selection method

We now calculate the $\Delta\eta$ for ^{85}Rb-^{87}Rb and ^{41}K-^{87}Rb using the specific $\phi_{\mathrm{B,ini},i}$ and $\phi_{\mathrm{W,evol},i}$ in Sec. IV B. The temperature of the atom clouds is set as 10 nK. Figure 5 displays the dependence of $\Delta\eta$ and β on the radius of the detection beams r_{det}. For both ^{85}Rb-^{87}Rb and ^{41}K-^{87}Rb, the magnitude of $\Delta\eta$ decreases with decreasing r_{det}. The detection ratio β of ^{41}K is lower than that of ^{85}Rb and ^{87}Rb due to the higher expansion rate of ^{41}K.

We also utilize the 10 individual random $\phi_{\mathrm{W,ini},i}$ and $\phi_{\mathrm{W,evol},i}$ to calculate the average values and standard deviations of $\Delta\eta$. The radii of the detection beams are set to make ^{85}Rb atoms have a detection ratio of 50%. At this situation, the detection ratio of ^{87}Rb and ^{41}K atoms are 50% and 23%, respectively. The calculation with the 10-nK atom clouds is shown in Table III. For ^{85}Rb-^{87}Rb and ^{41}K-^{87}Rb, the standard deviations of the $\Delta\eta$ induced by the overall $\phi_{\mathrm{R,nl},i}$ are 9.1×10^{-14} and 2.2×10^{-12}, respectively. The corresponding suppression ratios are 450 and 25.

Comparing with Table II, the suppression ratios are improved for about one order of magnitude. $\Delta\eta$ of ^{41}K-^{87}Rb induced by the $\phi_{\mathrm{B,evol},i}$ is -4.3×10^{-14}, which is about 50 times smaller than the value in Table II. We also calculate the $\Delta\eta$ for the 1-nK atom clouds with the same detection ratio; the standard deviations of $\Delta\eta$ induced by $\phi_{\mathrm{R,nl},i}$ for ^{85}Rb-^{87}Rb and ^{41}K-^{87}Rb are 1.3×10^{-14} and 3.0×10^{-13}, respectively, and the corresponding suppression ratios are 460 and 28.

V. CONCLUSION

We investigated the wave-front-aberration induced phase noise in ^{85}Rb, ^{87}Rb, and ^{41}K AI-based relative gravity measurement, as well as in ^{85}Rb-^{87}Rb and ^{41}K-^{87}Rb AI-based WEP tests. The influences of different phase terms of the Raman beams are analyzed and calculated in detail; the systematic error in relative gravity measurements and WEP test are simulated. We find that the gouy phase and the initial aberration phase are two majority factors that limit the error suppression ratio in WEP tests. We proposed an expansion rate selection method to improve the suppression ratio both for the average value and standard deviation for the WEP test experiment. By using this method and under certain simulated parameters, the deviations of WEP tests using 1-nK ^{85}Rb-^{87}Rb and ^{41}K-^{87}Rb are 1.3×10^{-14} and 3.0×10^{-13}, respectively. Better results can be obtained by improving the wave-front quality and utilizing the atom cloud with lower temperature. The analysis and suppression of wave-front-aberration phase

noise will be useful for the design of high-precision AI-based WEP tests both on ground and in space.

ACKNOWLEDGMENTS

We acknowledge the helpful discussion with Yuanzhong Zhang. This work was supported by the National Key Research and Development Program of China under Grant No. 2016YFA0302002, the Strategic Priority Research Program of the Chinese Academy of Sciences under Grant No. XDB21010100, and the National Natural Science Foundation of China under Grants No. 91536221, No. 11227803, and No. 11504411.

[1] M. A. Kasevich and S. Chu, Atomic Interferometry Using Stimulated Raman Transitions, Phys. Rev. Lett. **67**, 181 (1991).

[2] A. D. Cronin, J. Schmiedmayer, and D. E. Pritchard, Optics and interferometry with atoms and molecules, Rev. Mod. Phys. **81**, 1051 (2009).

[3] J. Wang, Precision measurement with atom interferometry, Chin. Phys. B **24**, 053702 (2015).

[4] Y. Bidel, O. Carraz, R. Charrière, M. Cadoret, N. Zahzam, and A. Bresson, Compact cold atom gravimeter for field applications, Appl. Phys. Lett. **102**, 144107 (2013).

[5] Z. K. Hu, B. L. Sun, X. C. Duan, M. K. Zhou, L. L. Chen, S. Zhan, Q. Z. Zhang, and J. Luo, Demonstration of an ultrahigh-sensitivity atom-interferometry absolute gravimeter, Phys. Rev. A **88**, 043610 (2013).

[6] B. Cheng, Z. Y. Wang, A. P. Xu, Q. Y. Wang, and Q. Lin, Rapid extraction of the phase shift of the cold-atom interferometer via phase demodulation, Chin. Phys. B **24**, 113704 (2015).

[7] F. Sorrentino, Q. Bodart, L. Cacciapuoti, Y. H. Lien, M. Prevedelli, G. Rosi, L. Salvi, and G. M. Tino, Sensitivity limits of a Raman atom interferometer as a gravity gradiometer, Phys. Rev. A **89**, 023607 (2014).

[8] M. J. Snadden, J. M. McGuirk, P. Bouyer, K. G. Haritos, and M. A. Kasevich, Measurement of the Earth's Gravity Gradient with an Atom-Interferometer-Based Gravity Gradiometer, Phys. Rev. Lett. **81**, 971 (1998).

[9] F. Pereira Dos Santos, Differential phase extraction in an atom gradiometer, Phys. Rev. A **91**, 063615 (2015).

[10] X. C. Duan, M. K. Zhou, D. K. Mao, H. B. Yao, X. B. Deng, J. Luo, and Z. K. Hu, Operating an atom-interferometry-based gravity gradiometer by the dual-fringe-locking method, Phys. Rev. A **90**, 023617 (2014).

[11] T. L. Guastavson, A. Landragin, and M. A. Kasevich, Rotation sensing with a dual atom-interferometer Sagnac gyroscope, Class. Quantum Grav. **17**, 2385 (2000).

[12] Z. W. Yao, S. B. Lu, R. B. Li, K. Wang, L. Cao, J. Wang, and M. S. Zhan, Continuous dynamic rotation measurements using a compact cold atom gyroscope, Chin. Phys. Lett. **33**, 083701 (2016).

[13] B. Canuel, F. Leduc, D. Holleville, A. Gauguet, J. Fils, A. Virdis, A. Clairon, N. Dimarcq, Ch. J. Bordé, and A. Landragin, Six-Axis Inertial Sensor Using Cold-Atom Interferometry, Phys. Rev. Lett. **97**, 010402 (2006).

[14] H. Müller, A. Peters, and S. Chu, A precision measurement of the gravitational redshift by the interference of matter waves, Nature (London) **463**, 926 (2010).

[15] G. Rosi, F. Sorrentino, L. Cacciapuoti, M. Prevedelli, and G. M. Tino, Precision measurement of the Newtonian gravitational constant using cold atoms, Nature (London) **510**, 518 (2014).

[16] J. B. Fixler, G. T. Foster, J. M. McGuirk, and M. A. Kasevich, Atom interferometer measurement of the Newtonian constant of gravity, Science **315**, 74 (2007).

[17] S. W. Chiow, S. Herrmann, S. Chu, and H. Müller, Noise-Immune Conjugate Large-Area Atom Interferometers, Phys. Rev. Lett. **103**, 050402 (2009).

[18] R. Bouchendira, P. Cladé, S. Guellati-Khélifa, F. Nez, and F. Biraben, New Determination of the Fine Structure Constant and Test of the Quantum Electrodynamics, Phys. Rev. Lett. **106**, 080801 (2011).

[19] H. Müller, S. W. Chiow, S. Herrmann, S. Chu, and K. Y. Chung, Atom-Interferometry Tests of the Isotropy of Post-Newtonian Gravity, Phys. Rev. Lett. **100**, 031101 (2008).

[20] L. Zhou, S. T. Long, B. Tang, X. Chen, F. Gao, W. C. Peng, W. T. Duan, J. Q. Zhong, Z. Y. Xiong, J. Wang, Y. Z. Zhang, and M. S. Zhan, Test of Equivalence Principle at 10^{-8} Level by a Dual-Species Double-Diffraction Raman Atom Interferometer, Phys. Rev. Lett. **115**, 013004 (2015).

[21] S. Fray, C. A. Diez, T. W. Hänsch, and M. Weitz, Atomic Interferometer with Amplitude Gratings of Light and its Applications to Atom Based Tests of the Equivalence Principle, Phys. Rev. Lett. **93**, 240404 (2004).

[22] A. Bonnin, N. Zahzam, Y. Bidel, and A. Bresson, Simultaneous dual-species matter-wave accelerometer, Phys. Rev. A **88**, 043615 (2013).

[23] D. Schlippert, J. Hartwig, H. Albers, L. L. Richardson, C. Schubert, A. Roura, W. P. Schleich, W. Ertmer, and E. M. Rasel, Quantum Test of the Universality of Free Fall, Phys. Rev. Lett. **112**, 203002 (2014).

[24] M. G. Tarallo, T. Mazzoni, N. Poli, D. V. Sutyrin, X. Zhang, and G. M. Tino, Test of Einstein Equivalence Principle for 0-Spin and Half-Integer-Spin Atoms: Search for Spin-Gravity Coupling Effects, Phys. Rev. Lett. **113**, 023005 (2014).

[25] X. C. Duan, X. B. Deng, M. K. Zhou, K. Zhang, W. J. Xu, F. Xiong, Y. Y. Xu, C. G. Shao, J. Luo, and Z. K. Hu, Test of the Universality of Free Fall with Atoms in Different Spin Orientations, Phys. Rev. Lett. **117**, 023001 (2016).

[26] A. Bonnin, N. Zahzam, Y. Bidel, and A. Bresson, Characterization of a simultaneous dual-species atom interferometer for a quantum test of the weak equivalence principle, Phys. Rev. A **92**, 023626 (2015).

[27] D. N. Aguilera, H. Ahlers, B. Battelier *et al.*, STE-QUEST-test of the universality of free fall using cold atom interferometry, Class. Quantum Grav. **31**, 115010 (2014).

[28] T. Lévèque, A. Gauguet, F. Michaud, F. Pereira Dos Santos, and A. Landragin, Enhancing the Area of a Raman Atom Interferometer Using a Versatile Double-Diffraction Technique, Phys. Rev. Lett. **103**, 080405 (2009).

[29] E. Giese, A. Roura, G. Tackmann, E. M. Rasel, and W. P. Schleich, Double Bragg diffraction: A tool for atom optics, Phys. Rev. A **88**, 053608 (2013).

[30] A. Sugarbaker, S. M. Dickerson, J. M. Hogan, D. M. S. Johnson, and M. A. Kasevich, Enhanced Atom Interferometer Readout Through the Application of Phase Shear, Phys. Rev. Lett. **111**, 113002 (2013).

[31] L. Zhou, Z. Y. Xiong, W. Yang, B. Tang, W. C. Peng, K. Hao, R. B. Li, M. Liu, J. Wang, and M. S. Zhan, Development of an atom gravimeter and status of the 10-meter atom interferometer for precision gravity measurement, Gen. Relativ. Gravit. **43**, 1931 (2011).

[32] J. Hartwig, S. Abend, C. Schubert, D. Schlippert, H. Ahlers, K. Posso-Trujillo, N. Gaaloul, W. Ertmer, and E. M. Rasel, Testing the universality of free fall with rubidium and ytterbium in a very large baseline atom interferometer, New J. Phys. **17**, 035011 (2015).

[33] J. Williams, S. W. Chiow, N. Yu, and H. Müller, Quantum test of the equivalence principle and space-time aboard the International Space Station, New J. Phys. **18**, 025018 (2016).

[34] A. Louchet-Chauvet, T. Farah, Q. Bodart, A. Clairon, A. Landragin, S. Merlet, and F. Pereira Dos Santos, The influence of transverse motion within an atomic gravimeter, New J. Phys. **13**, 065025 (2011).

[35] V. Schkolnik, B. Leykauf, M. Hauth, C. Freier, and A. Peters, The effect of wavefront aberrations in atom interferometry, Appl. Phys. B **120**, 311 (2015).

[36] M. K. Zhou, Q. Luo, L. L. Chen, X. X. Duan, and Z. K. Hu, Observing the effect of wave-front aberrations in an atom interferometer by modulating the diameter of Raman beams, Phys. Rev. A **93**, 043610 (2016).

[37] E. Collett and R. Alferness, Depolarization of a laser beam in a turbulent medium, J. Opt. Soc. Am. **62**, 529 (1972).

[38] X. Chen, J. Q. Zhong, H. W. Song, L. Zhu, J. Wang, and M. S. Zhan, Proportional-scanning-phase method to suppress the vibrational noise in nonisotope dual-atom-interferometer-based weak-equivalence-principle-test experiments, Phys. Rev. A **90**, 023609 (2014).

[39] G. T. Foster, J. B. Fixler, J. M. McGuirk, and M. A. Kasevich, Method of phase extraction between coupled atom interferometers using ellipse-specific fitting, Opt. Lett. **27**, 951 (2002).

[40] J. K. Stockton, X. A. Wu, and M. A. Kasevich, Bayesian estimation of differential interferometer phase, Phys. Rev. A **76**, 033613 (2007).